1

M2 Monthly and annual mode 1 and mode 2 internal tide atlases from altimetry data and MIOST: focus on the Indo-Philippine Archipelago and the region off the Amazon shelf.

Michel Tchilibou[1], Simon Barbot[2], Loren Carrere[1], Ariane Koch-Larrouy[2], Gérald Dibarboure[3] and Clément Ubelmann[4]

[1] Collecte Localisation Satellites, 31520 Ramonville-Saint-Agne, France

[2] Université de Toulouse, LEGOS (CNES/CNRS/IRD/UT3), 31400 Toulouse, France

[3] Centre National d'Etude Spatiales, 31400, Toulouse, France

[4] Datlas, Grenoble, France

Correspondence to: Michel Tchilibou (mtchilibou@groupcls.com)

Abstract

The M2 MIOST24 (Multivariate Inversion of Ocean Surface Topography 2024) internal tide atlases are available in annual (MIOST24a) and monthly (MIOST24m) regional versions for modes 1 and 2 in the Indo-Philippine archipelago and the region off the Amazon shelf. They are derived from 25 years (1993-2017, period 1) of sea level anomalies (SLA) from altimetry observations. Compared to MIOST22, MIOST24 incorporates M2 modes 1 and 2 wavelengths based on monthly stratification profiles from GLORYS12v1 (1993-2020). The differences between MIOST24a and MIOST22a lead to RMSE (Root Mean Square Error) of up to 3 cm, reflecting amplitude changes, while the RMSE between MIOST24a and HRET (High-Resolution Empirical Tide) indicate both amplitude and phase differences. MIOST24m highlights significant monthly variability of M2 internal tides in the Indo-Philippine archipelago and off the Amazon shelf. In the Amazon region, the internal tide propagates far offshore from March to June but is blocked closer to the coast from August to December. For both regions, mode 1 monthly variability is mainly phase-related, while mode 2 is more amplitude-dependent. Variance reductions of SLA show that MIOST24m outperforms MIOST24a, MIOST22a and HRET on period 1 in the two regions of interest, and on the Amazon region in period 2 (2018-2023). Monthly atlases are therefore recommended to correct the internal tides of the SLA used to derive them. All these results support the development of an improved MIOST24 global atlas.

Introduction

Since the early 1990s and the launch of the TOPEX/Poseidon mission, spatial altimetry has provided an independent source of measurements of ocean surface topography. These measurements are essential for a better understanding of ocean surface dynamics, deep ocean circulation and their impact on climate (Escudier et al., 2017). Significant progress has been made in the processing and reprocessing of altimetry data (Dibarboure et al. 2011, Ablain et al., 2015, Pujol et al., 2016, Pujol et al.,2023). Today, more than 30 years of observations are available. They can be used directly or indirectly (model constraints, data assimilation) to generate global atlases of barotropic tides (Stammer et al., 2014, Carrere et al., 2016, Lyard et al., 2020, Lyard et al.,2024 Desai and Ray, 2014, Egbert and Erofeeva, 2002) and baroclinic tides, also known as internal tides (Dushaw et al., 2011; Dushaw, 2015, Zhao et al.,2012, Ray and Zaron, 2016; Zaron et al., 2019, Ubelmann et al., 2022). In turn, these tidal atlases are used as geophysical corrections in the Data Unification and Altimeter Combination System (DUACS) chain to compute the Sea Level Anomaly (SLA) along the altimeter tracks (L3 product) and on regular horizontal grids (L4 product).

41   Internal tide (IT) atlases have been included in the geophysical corrections of the altimetry dataset since
42 the transition from version DT2018 to DT2021 in the DUACS processing chain (Sanchez-Roman et al., 2021;
43 Lievin et al., 2020; Faugere et al., 2022). The internal tide model currently used as a reference in DUACS is
44 HRETv8.1 (High-Resolution Empirical Tide 8.1, HRET in the rest of the paper) by Zaron (2019). Several global
45 atlases exist as described in (Carrère et al., 2021), such as those by Zhao (Zhao et al., 2012, 2018, 2019, 2021)
46 or MIOST (Multivariate Inversion of Ocean Surface Topography; Ubelmann et al., 2021, 2022). The MIOST
47 atlas of Ubelmann et al. (2022), like the Zhao atlases, uses mode 1 and 2 theoretical internal tide wavelengths'
48 climatologies to extract the internal tide signal from the altimetric SLA. For the 2022 version of the MIOST
49 atlas, Ubelmann et al. (2022) use the first Rossby deformation radius climatology from Chelton et al. (1998)
50 as an approximation of the mode 1 wavelength and divide it by two to approximate the mode 2 wavelength.
51 These approximations are not always accurate because each baroclinic mode has characteristics influenced
52 by ocean stratification (Gerkerma et al., 2004). Moreover, the climatology of Chelton et al. (1998) is based
53 on a very different period from the 1993 - 2017 period of the altimetry data used by Ubelmann et al. (2022),
54 which could lead to inaccuracies in the location and amplitude of internal tides. The first objective of this
55 study is to propose a 2024 version of MIOST IT atlas based on more appropriate mode 1 and 2 wavelengths,
56 thus overcoming the deficiencies of the wavelengths prescribed in Ubelmann et al. (2022).

57   The second objective of this study concerns the monthly variability of the internal tide and the relevance
58 of replacing the HRET internal tide atlas with monthly atlases in the DUACS chain. Altimetry-derived internal
59 tide atlases only include the stationary (or coherent, or phase-lock) part of the internal tides. The coherent
60 and incoherent (non-stationary) internal tides both vary with stratification and the interactions of the internal
61 tides with the ocean circulation, including mesoscale eddies (Tchilibou et al., 2020; Duda et al.,2018; Dunphy
62 et al., 2014). This variability is not considered in annual atlases such as HRET, which use the altimetry
63 database as a single set. Zhao (2021) builds subsets of altimetry data over the four meteorological seasons
64 and shows that seasonal atlases perform better in tropical regions but with some limitations. In this study,
65 we extend the question of internal tide variability to the monthly scale, focusing on the M2 wave in the Indo-
66 Philippine archipelago (Figure 1a) and the region of the Amazon shelf in the tropical Atlantic (Figure 1b).

67
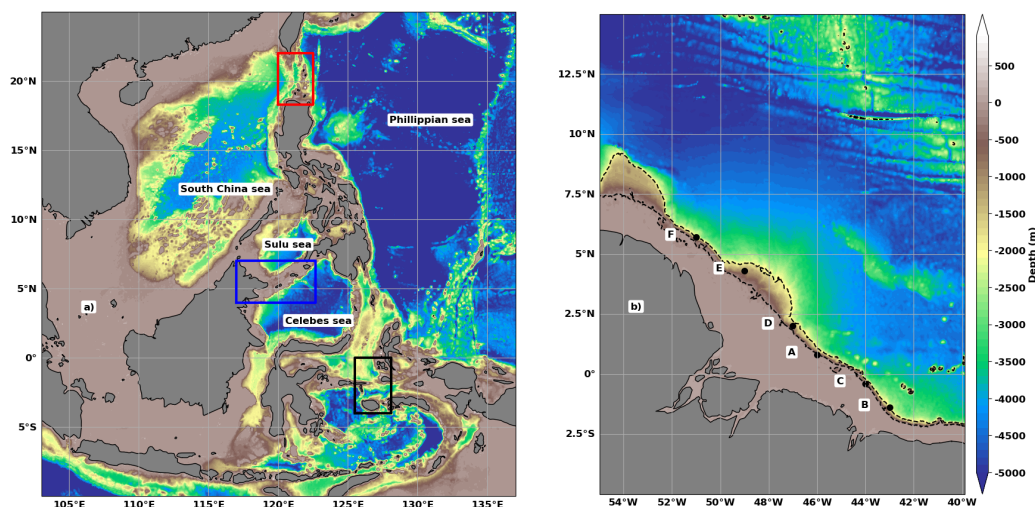
Figure 1: Bathymetric depth (in m) in the Indo-Philippine archipelago (a) and the region off the Amazon shelf
(b). The major internal tide generation areas are indicated by red (Luzon Strait), blue (Sulu Island Chain) and
black (Seram Sea) boxes for the Indo-Philippine archipelago and by the letters A-F for the Amazon shelf-
break.

72   These two tropical regions are chosen because they are hotspots of M2 internal tide generation and the
73   site of high M2 internal tide variability (Jan et al.,2008; Muller et al.,2012; Ray and Zaron 2011, Niwa and
74   Hibiya 2001, 2004 and 2014, Arbic et al.,2012; Nugroho et al., 2018; Zhao and Qui 2023; Pickering et al.,2015;
75   Rainville et al.,2013; Tchilibou et al., 2022; Assene et al., 2024). In addition, the Indo-Philippine archipelago
76   is a transit zone between the Pacific and Indian Oceans (Sprintall et al., 2014; Hurlburt et al., 2011), and the
77   tide-induced mixing there affects the coupled ocean-atmosphere system and thus the global climate system
78   (Koch-Larrouy et al., 2010). More details on these two regions can be found in Nugroho (2018) and Tchilibou
79   et al. (2022). The paper is divided into 5 sections. In section 1 we give an overview of HRET, compare the
80   wavelengths' bases of the 2022 and 2024 versions of MIOST-IT, and present the altimetry data and how they
81   are organized to derive the annual (classical) and monthly atlases. In section 2, the annual atlases of MIOST-
82   IT 2022 and 2024 are compared qualitatively with HRET. The efficiency of the monthly atlases in correcting
83   for internal tides in the altimetry data is analyzed in section 4, and the paper is concluded in section 5.

84   **1- Internal tide atlases and data:**
85
86   In this section, we describe the different internal tide atlases developed within the study (MIOST24) as
87   well as the datasets used for computation, and the other atlases used for comparison (MIOST22 and
88   HRET).
89
90
91   **1.1- HRET**
92
93   HRET (for HRETv8.1; Zaron 2019) is an empirical atlas of internal tides at the M2, S2, K1 and O1 frequencies,
94   developed from the analysis of the 1993 to 2017 (25 years) exact repeat mission altimetry data (Topex, Jason
95   1 to 3, ERS, Envisat, Saral AltiKa and the GEOSAT follow-on). The method used to construct the HRET internal
96   tide atlas involves a local two-dimensional Fourier analysis of the along-track data, and a least-squares fit by
97   a second-order polynomial. HRET is provided on a horizontal grid of 0.05°X0.05° (1/20°) and includes modes
98   1 and 2. A mask is applied in the regions where the amplitude of the internal tides is very noisy.
99
100   **1.2- MIOST22 and MIOST24 mode 1 and 2 wavelengths for M2:**
101
102   MIOST is an empirical atlas of internal tides obtained by a single inversion that simultaneously separates
103   mesoscale and internal tides (modes 1 and 2) from altimetry observations (Ubelmann et al., 2022). The
104   2022 and 2024 versions of MIOST-IT atlases are hereafter referred to as MIOST22 and MIOST24. The
105   suffixes 'a' and 'm' are used to distinguish between annual (e.g. MIOST24a) and monthly (e.g. MIOST24m)
106   MIOST atlases.
107
108   In MIOST, mesoscales are expressed as a reduced wavelet basis. Internal tides are defined by a plane-
109   wave basis according to the dispersion relation (e.g. Rainville et Pinkel, 2006) given in Equation 1, where f
110   is the Coriolis parameter, λ_n, C_n and ω are the wavelength, eigenspeed and pulsation of the internal tides
111   of mode n, respectively.

$$\lambda_n = \frac{2\pi C_n}{\sqrt{\omega^2 - f^2}}, (1)$$

114   As mentioned in the introduction, for MIOST22 the wavelength of mode 1 corresponds to the first Rossby
115   deformation radius and the wavelength of mode 2 is half the wavelength of mode 1. For MIOST24, mode 1
116   and 2 wavelengths are determined independently by solving the eigenvalue equation (Eq 2; Gill, 1982) with
117   the boundary conditions $\phi_n(0) = \phi_n(H) = 0$, where H is the ocean depth and $\phi_n(z)$ the modal vertical
118   structure.

119
$$\frac{\partial^2 \phi_n(z)}{\partial z^2} + \frac{N(z)^2}{C_n^2}\phi_n = 0, (2)$$

120   The $N(z)$ stratification profiles required for equation 2 are computed from the 1993 - 2020 monthly
121   climatologies of the potential temperature and salinity fields from the GLORYS12v1 reanalysis
122   (https://doi.org/10.48670/moi-00021, last accessed 30/07/2024). GLORYS12v1 is a global CMEMS
123   (Copernicus Marine Environment Monitoring Service) product with a horizontal resolution of 1/12° and 50
124   levels. It is based on an eddy-resolving NEMO platform assimilating along tracks altimetric SLA, satellite sea
125   surface temperature observations and in situ vertical temperature and salinity profiles (Argo, moorings, etc.).
126   The GLORYS12v1 reanalyses are used as they are to calculate $N(z)$ and derive the monthly mode 1 and 2
127   wavelengths of the M2 internal tides required for MIOST24m. The MIOST24a atlas requires annual
128   wavelengths, obtained using $N(z)$ derived from the annual mean of GLORYS12v1 fields. The annual
129   wavelengths used for MIOST22a and MIOST24a and the standard deviations of the monthly wavelengths
130   used for MIOST24m are shown in Figure 2 for the Indo-Philippine Archipelago and Figure 3 for the region off
131   the Amazon shelf.

132   In the Indo-Philippine archipelago, the annual mode 1 (Figures 2a and 2c) and mode 2 (Figures 2b and 2d)
133   M2 wavelengths used for MIOST22 (Figures 2a and 2b) are generally larger than those used for MIOST24
134   (Figure 2c and 2d). The differences can be up to 10 km and are quite pronounced south of the Philippine Sea,
135   in the South China Sea, in the Celebes Sea and the Banda Sea. Only in the Sulu Sea do MIOST24 wavelengths
136   exceed those of MIOST22. The simplified approximation that the wavelength of mode 2 is half the one of
137   mode 1, used for MIOST22, implies that the spatial distributions of the two modes are equivalent (Figure 2a
138   and 2b). We assume that the locations of the maximum wavelengths in mode 1 also correspond to the
139   locations of the longest wavelengths in mode 2, and similarly for the locations of the shortest wavelengths.
140   This is not the case when looking at the MIOST24 wavelength maps for modes 1 (Figure 2c) and 2 (Figure 2d).
141   In the Sulu Sea, the mode 2 wavelengths of MIOST22 are about 50 km, *i.e.* among the shortest, while in
142   MIOST24 they are of the order of 80 km, *i.e.* the highest.
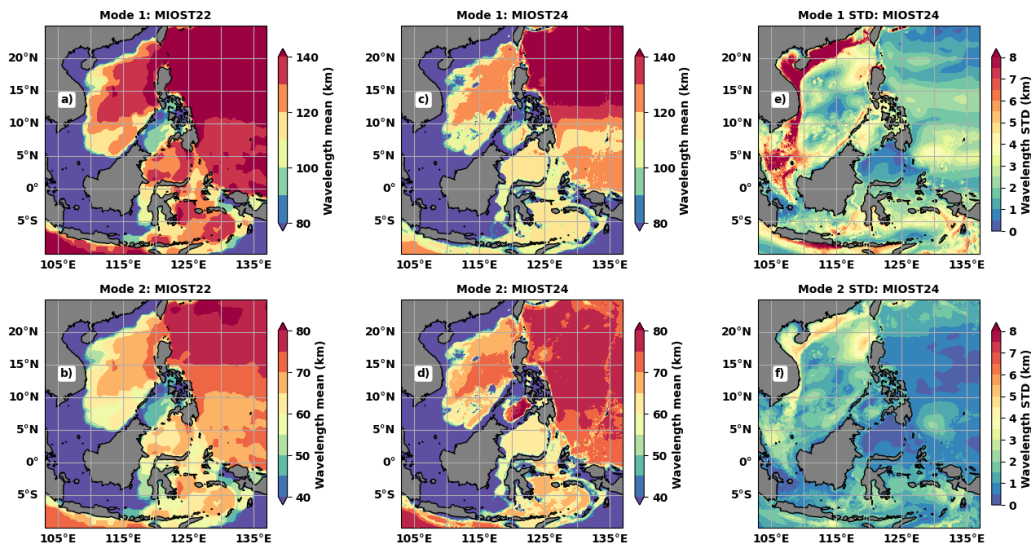

143

144   **Figure 2:** M2 wavelengths values (a-d, in km) and standards deviations (e-f, in km) in the Indo-Philippine
145   archipelago: (a) mode 1 and (b) mode 2 annual values used for MIOST22a, (c) mode 1 and (d) mode 2 annual
146   values used for MIOST24a, standard deviation of (e) mode 1 and (f) mode 2 monthly wavelengths used for
147   MIOST24m.

148   Off the Amazon shelf, the M2 wavelengths of MIOST22 and MIOST24 show differences in both spatial
149 distribution and values (Figure 3). In MIOST22, mode 1 (Figure 3a), and mode 2 (Figure 3b), the wavelength
150 gradient is positive from offshore to about 7°N. Thereafter the wavelengths decrease slightly. In MIOST24
151 the structures are more homogeneous (Figure 3c and 3d). Outside the continental shelf, mode 1 wavelengths
152 (Figure 3c) are mostly between 100 and 110 km, while they exceed 120 km in MIOST22 (Figure 3a). For mode
153 2 (Figure 3d), the dominant structure corresponds to wavelengths between 65 and 70 km, while in MIOST22
154 the space bounded by this structure also includes a short-wavelength zone between 60 and 65 km (Figure
155 3c). As in the Indo-Philippine archipelago, there is no direct relationship between the spatial distributions of
156 mode 1 and 2 annual wavelengths in MIOST24. This confirms that the wavelength characteristics are specific
157 to each mode.

158
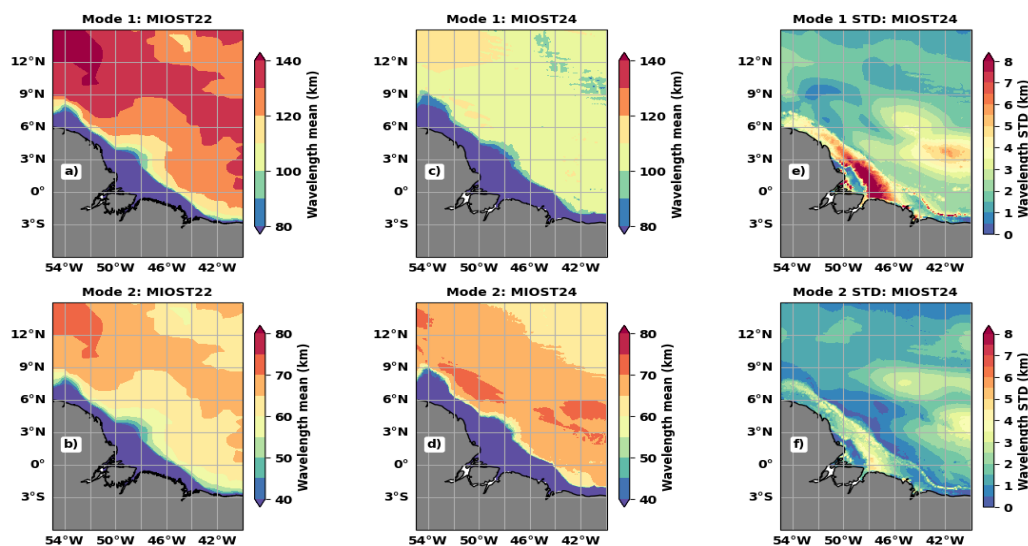
160 **Figure 3:** As Figure 2 for the region off the Amazon shelf.

161   The differences between the wavelengths of MIOST22 and MIOST24 reflect the differences between the
162 stratifications and therefore between the climatological eigenspeed used in each case. According to Equation
163 1, a velocity difference of 0.1 m/s corresponds to 4 to 5 km shift in the wavelengths for the latitudes of
164 interest here, between 10°S and 20°N. We have found differences of up to 0.5 m/s between the eigenspeed
165 of MIOST22 and MIOST24 (not shown). Despite the differences with the MIOST22 wavelengths, we remain
166 confident about the MIOST24 wavelengths as they are close to those used by Zhao (2018), which is based on
167 the same method but on the stratification from the World Ocean Atlas 2013 climatology.

168   The standard deviations of the monthly M2 wavelengths used to derive the MIOST24m atlases are shown
169 for modes 1 and 2 in the last column of Figures 2 and 3. In both regions, the M2 wavelength variation over
170 the year is up to 5 km for mode 1 (Figures 2e and 3e) and 3 km (Figures 2f and 3f) for mode 2 in the deep
171 ocean. On the continental shelves the M2 wavelength variation is up to 8 km for mode 1 and 5 km for mode
172 2. In the Luzon Strait (Figure 2), wavelength variations are more pronounced in the western part, which opens
173 to the South China Sea, than in the eastern part, which opens to the Philippine Sea. Wavelengths are relatively
174 stable in the Celebes Sea (Figure 2), with monthly variations of less than 2 km for mode 1 and less than 1 km
175 for mode 2. Outside the continental shelf, wavelengths vary more in the eastern part of the Amazon region
176 (Figure 3). The wavelength variability would also have been biased if the mode 2 wavelengths had been taken

177   to be half the mode 1 wavelength as in MIOST22. For example, south of the Philippine Sea, mode 1
178   wavelengths vary between 1 and 4 km (Figure 2e), while mode 2 (Figure 2f) is relatively stable (less than 1
179   km). In addition, for the boxes in Figure 1a and the region off the Amazon shelf, the spatial means of monthly
180   wavelengths have been plotted and presented in the Appendix to illustrate further the annual cycle of mode
181   1 and 2 wavelengths.

182   **1.3- Database organization for annual and monthly atlases:**

183   In this study, we use Level 3 along-track data with a resolution of 1 Hz (about 7 km), processed according
184   to the DT2024 protocol (Kocha et al., 2023) and available on Copernicus website (see link in Data availability).
185   The HRET correction is reintroduced to obtain an SLA with the full internal tide signal. As in MIOST22, data
186   are from the Topex/Poseidon, Jason-1, Jason-2, Jason-3, Sentinel-3A, Sentinel-3B, Saral/AltiKa, Cryosat-2,
187   ERS-1, ERS-2, Envisat, Geosat Follow-On and HY-2A altimetry missions. The altimetry SLAs are selected from
188   1993 to 2023 and divided into two periods. The MIOST24a and MIOST24m atlases are derived from the SLA
189   over "period 1" between January 1993 and December 2017, as are MIOST22 and HRET. The "period 2" from
190   January 2018 to December 2023 is used for validation as independent measurements. The validation consists
191   of an inter-comparison of the levels of altimetry residual SLA after applying the internal tide corrections using
192   either the HRET, MIOST22 or MIOST24 atlases.

193   The 25 years of SLA data from period 1 are used as a single set to derive the annual MIOST24a atlas
194   (stationary part over 25 years). Period 1 and 2 SLA data are divided into monthly subsets to derive the
195   MIOST24m atlas and to validate the four atlases. Due to tidal aliasing in the altimetry observations and the
196   low repeatability of the satellites, the monthly subsets are formed by overlapping the month in question by
197   15 days on each side. For example, the SLA subset data for April is defined with SLAs from 16 March to 15
198   May. Finally, the monthly time series covers about 4 years (1500 days) of observations (60 days per year over
199   25 years), which is a minimum for separating the S2 and M2 harmonics for the Topex/Poseidon and Jasons
200   missions, whose reference orbit has a period of 9.92 days. After analysis of the altimetry data, the MIOST24a
201   and MIOST24m M2 atlases are produced on 1/20° horizontal grids, the same resolution as HRET, while
202   MIOST22 was produced on a 1/10° grid. The HRET mask is applied to the MIOST atlas to harmonize the
203   comparisons.

204   **2-   MIOST24a M2 atlas, comparison with MIOST22 and HRET:**
205

206   This section compares the annual M2 atlas MIOST24a with the annual M2 atlases MIOST22a and HRET.
207   First, the internal tide amplitude maps M2 are compared. Then, considering the amplitudes (A, A_m), and
208   phases (φ, φ_m), the Root Mean Square Error (RMSE) between MIOST24 and MIOST22 or MIOST24 and HRET
209   is calculated according to equation 3 for a more complete quantification of the distance between the atlases.
210   Equation 3 can be rewritten as equation 4, where the terms on the right indicate the contribution of the
211   amplitude differences to the RMSE (Ac) and the contribution of the phase differences to the RMSE (Pc). The
212   phase differences contribute more to the RMSE when the ratio of the second term to the first term on the
213   right is greater than 1 ($Pc / Ac > 1$, in equation 5). This ratio is referred to as the rate of the contributions
214   to the RMSE (Rc) and is evaluated for locations with amplitude differences greater than 3 mm, more precisely
215   $(A - A_m)^2 > 0.1$, and this is to avoid noise effects on the ratio.

$$RMSE = \sqrt{\frac{1}{2}|Ae^{i\varphi} - A_m e^{i\varphi_m}|^2}, \ (3)$$

$$2RMSE^2 = (A - A_m)^2 + 2AA_m (1 - cos(\varphi - \varphi_m)), (4)$$

$$Rc = Pc / Ac = 2AA_m (1 - cos(\varphi - \varphi_m)) / (A - A_m)^2, (5)$$

219   The amplitudes of the total internal tides (including mode 1 and 2) and mode 2 internal tides, as obtained
220   for MIOST24a, are shown in Figures 4a and 4b, respectively, for the Indo-Philippine archipelago. Three main
221   areas stand out for their maximum amplitude of more than 8 cm for the total internal tides and more than 4
222   cm for mode 2: the Luzon Strait, the Sulu Island chain and the Serem Sea. These are the main sources of
223   internal tides in this part of the ocean. Once generated, the internal tides propagate through the various seas
224   of the archipelago. From the Luzon Strait, the intrusion of the internal tides is stronger to the east in the
225   Philippine Sea compared to the west in the South China Sea (Figure 4a).

226   MIOST24a (Figure 4a) agrees with MIOST22a (Figure 4c) and HRET (Figure 4d) in the spatial distribution of
227   the M2 internal tide amplitude. Compared to the latter two atlases, MIOST24a shows stronger amplitudes
228   and well-defined small-scale structures, because mode 2 is better defined in MIOST24a. On the RMSE maps,
229   the differences between MIOST24a and MIOST22a are 1-2 cm south of 5°N and around Luzon Strait (Figure
230   4e). For the same locations, the RMSE between MIOST24a and HRET (Figure 4f) increases to 3 cm and non-
231   zero RMSE marks are more visible in the Philippine Sea. The spatial mean of Rc is 1.36 for the RMSE between
232   MIOST24a and MIOST22a, indicating that the atlases differ mainly by their phases. For HRET, the spatial mean
233   of Rc is 1.06, thus amplitudes and phases contribute equally to the differences between MIOST24a and HRET.
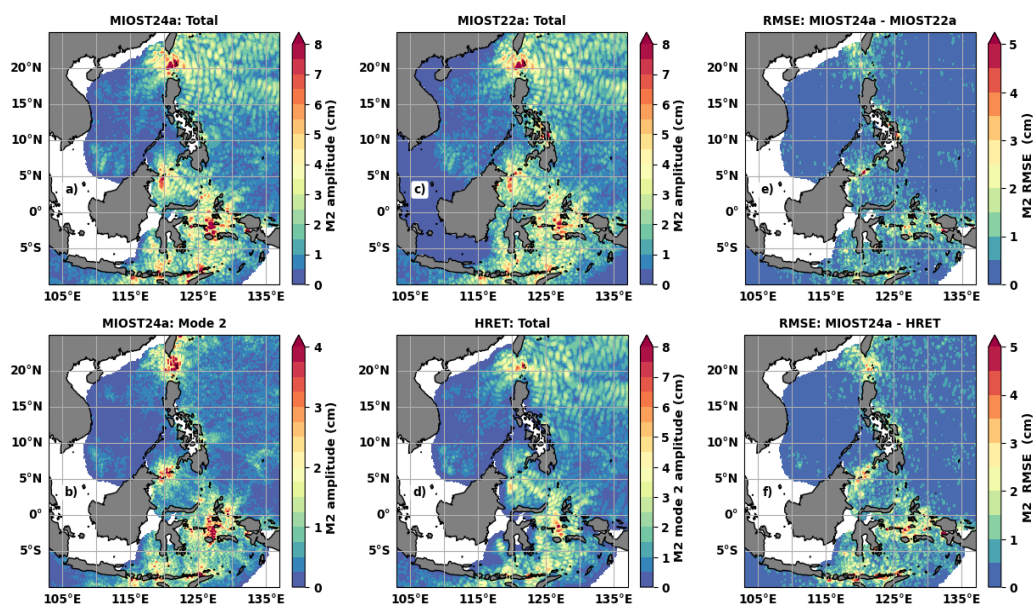

Figure 4: Amplitude (a-d, in cm) and RMSE (e-f, in cm) of the M2 internal tides in the Indo-Philippine
Archipelago. Amplitudes are shown for (a) MIOST24a total internal tides, (b) MIOST24a mode 2 internal tides,
(c) MIOST22a total internal tides and (d) HRET total internal tides. The RMSE is computed for (e) MIOST22a
and (f) HRET against MIOST24a. White corresponds to the HRET mask applied to MIOST24 to facilitate
comparison.

240   In the region off the Amazon shelf (Figure 5), MIOST24a is also characterized by offshore propagation of
241   internal tides. Two lines of maximum internal tides are distinguishable south of 2.5°N (Figure 5a), and the
242   third is less clear. Mode 2 from the Amazon shelf-break can be seen following these lines (Figure 5b). Again,
243   the amplitude of the M2 internal tides is stronger in MIOST24a, but the atlas matches MIOST22a (Figure 5c)
244   and HRET (Figure 5d), even if the latter shows smoother structures. As in the Indo-Philippine archipelago, the
245   RMSEs between MIOST24a and the other two atlases are mostly lower than 2 cm but exceed 3 cm at a few
246   locations (Figures 5e and 5f). The MIOST24a atlas differs more from MIOST22a (Figure 5e) and HRET (Figure

247 5f) in the first 100 to 200 km from the shelf break. The RMSEs are characterized by small scale structures in
248 this zone where the mode 2 amplitude is maximum. This suggests that the RMSEs reflect the changes
249 associated with improved mode 2 in MIOST24. The spatial means of Rc are 1.35 and 0.69 for the RMSE
250 between MIOST24a and MIOST22a and HRET, respectively. In this region, the phase differences are dominant
251 between MIOST22a and MIOST24a, while the amplitude differences are dominant between MIOST24a and
252 HRET.
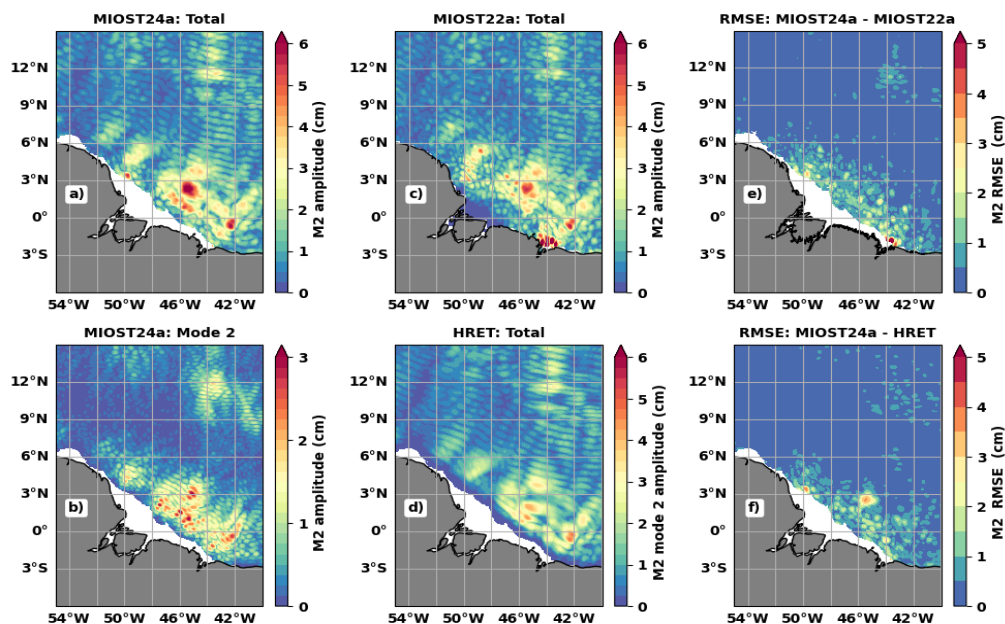
253

254 **Figure 5:** As Figure 4 for the region off the Amazon shelf.

255 **3- MIOST24m M2 atlases, the monthly variability of the internal tide:**
256

257 As a reminder, the MIOST24m monthly atlases are derived from the monthly climatology of M2
258 wavelength (Section 1.2) and monthly subsets of the altimetry data (Section 1.3). Monthly mode 1 and 2
259 atlases for April, July, September and December have been selected to illustrate the different propagation
260 situations and changing amplitudes of internal tides that occur throughout the year. The RMSE is calculated
261 between the monthly atlases MIOST24m and the annual atlas MIOST24a. The annual cycles of the spatial
262 mean of the RMSE and Rc are used to investigate the monthly variability of the M2 internal tide.

263 In the Indo-Philippine archipelago (Figure 6), the propagation of the mode 1 internal tides towards the
264 Philippine Sea is most pronounced in the early months of the year, such as April (Figure 6a) and in December
265 (Figure 6d). For the rest of the year, the structure of the internal tides is distorted quite rapidly, as in June
266 (Figure 6b) and September (Figure 6c). In the South China Sea and the rest of the archipelago, the amplitude
267 and trajectories of the internal tides vary. Mode 2 variability is more characterized by amplitude variations
268 (Figure 6 e-h). In the first half of the year in the region off the Amazon shelf (Figure 7), the internal tides of
269 mode 1 propagate freely from the Amazon shelf-break towards the open ocean, as in April (Figure 7a) and
270 June (Figure 7b). In the second half of the year, mode 1 has difficulty crossing 5°N, as in September (Figure
271 7c) and December (7d). The amplitude variations of mode 2 (Figure 7 e-h) are also easily distinguishable in
272 this region.
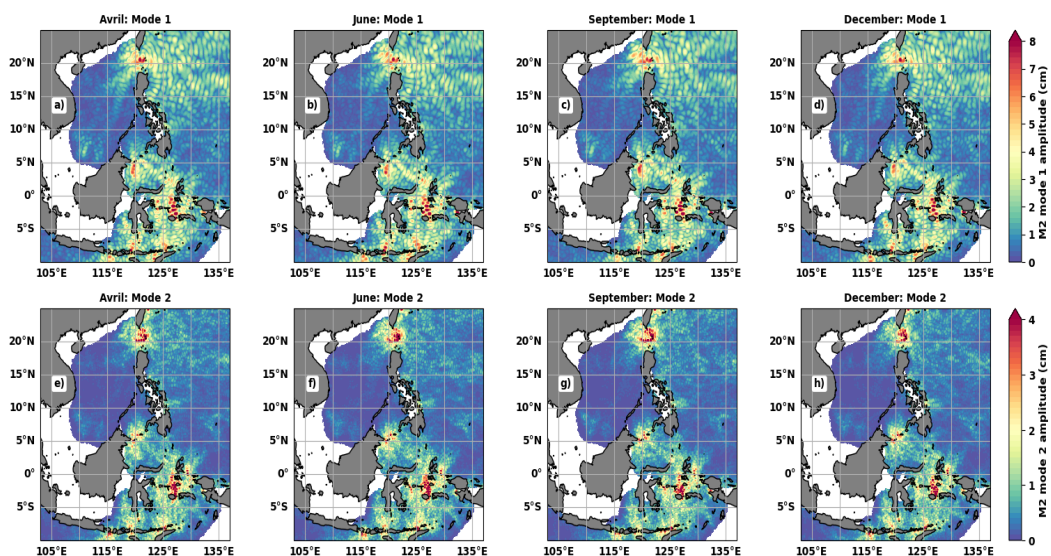
Figure 6: MIOST24m M2 mode 1 (top) and mode 2 (bottom) amplitudes (in cm) for Avril (a and e), June (b and f), September (c and g) and December (d and h).
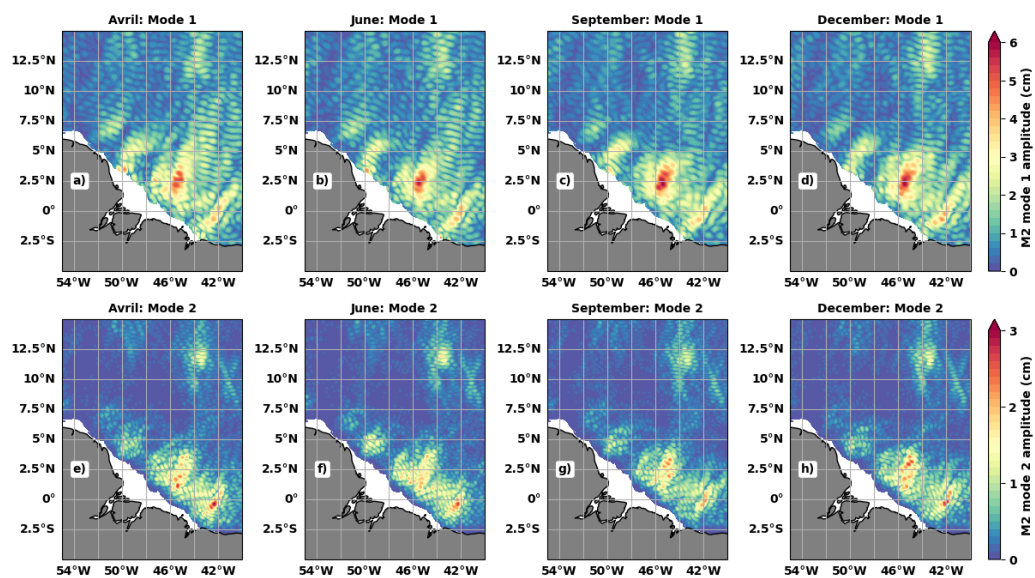

Figure 7: As Figure 6 for the region off the Amazon shelf.

The annual cycles of the spatial mean of monthly RMSE (Figure 8) of the total internal tides (in red), mode 1 (in blue) and mode 2 internal tides (in green) confirm that the internal tides are not constant throughout the year. For the two regions of interest, the annual cycle of the spatial mean of the RMSE of the total internal tides is like that of the mode 1 internal tides. The largest discrepancies between the annual MIOST24a atlas and the monthly MIOST24m atlases of the total and mode 1 internal tides occur in January, August and December in the Indo-Philippine archipelago (Figure 8a). Monthly and annual atlases are closest in May

284   (Figure 8 a). The annual cycle of the spatial mean of the RMSE for Mode 2 is consistent with that of mode 1,
285   although there is a one-month lag between the maximum peaks of mode 1 and mode 2 (Figure 8a).

286   Off the Amazonian shelf (Figure 8b), the annual cycle of the spatial mean of the RMSE of the total and mode
287   1 internal tide is bimodal, with the minimum of July dividing the year into two parts. For mode 2, the RMSE
288   is relatively constant between January and April, so on average mode 2 internal tides barely vary during these
289   months. From April to December, the RMSE cycle is bimodal as for mode 1, with peaks in June and September.
290   The bimodal shape of the annual cycle of the spatial mean of the RMSE is consistent with the behavior of the
291   M2 amplitudes during the year, as partially shown in Figure 7. It is also reminiscent of the distinction made
292   by Tchilibou et al, 2022, which separates the MAMJJ (March to July) months of high internal tides coherence
293   from the ASOND (August to December) months of high internal tides incoherence due to the increase of the
294   eddy kinetic energy.
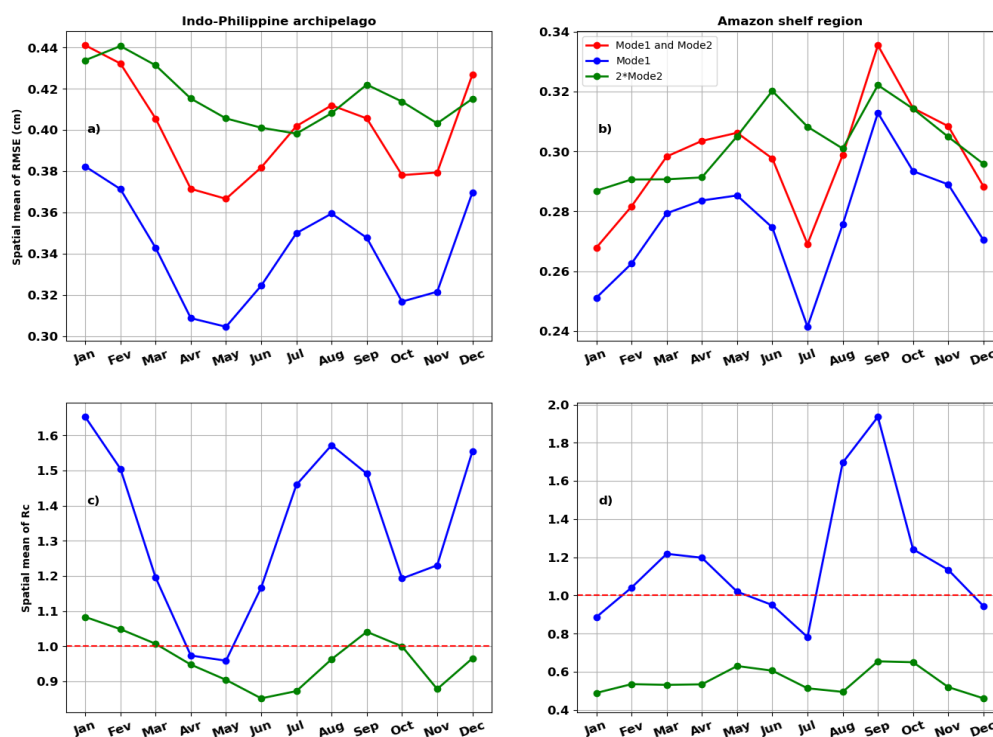
295

Figure 8: Annual cycle of the spatial mean of (top) the monthly RMSE (in cm) and (bottom) the monthly rate
of the contributions to the RMSE (Rc) in the Indo-Philippine Archipelago (a and c) and the region off the
Amazon shelf (b and d). The RMSE is calculated for the total internal tide (modes 1 and 2, in red), mode 1 (in
blue) and mode 2 (in green). Note that the RMSE for mode 2 has been multiplied by 2 to improve visibility.
The rate of the contributions to the RMSE (Rc) is evaluated following equation 5 and for locations with
amplitude differences greater than 3 mm.

302   The monthly spatial mean of Rc for mode 1 is greater than 1 for most of the year, except for April and May
303   in the Indo-Philippine Archipelago (Figure 8c) and especially for July in the region off the Amazon shelf (Figure
304   8d). The latter months are those with the lowest RMSE (Figure 8a-b). Thus, the RMSEs between the monthly
305   MIOST24m and annual MIOST24a mode 1 atlases express differences in amplitude for the month with the
306   minimum RMSE, but in general over the year, differences in phase and therefore in the internal tides
307   structures between the atlases. For Mode 2, Rc indicates that the RMSE reflects that amplitude differences

308 predominate over phase differences in the two regions. Except, of course, for January, February and
309 September in the Indo-Philippine archipelago, for which the RMSE is maximum (Figure 8a).

310 Examples of the annual cycle of the M2 internal tides amplitude are shown in the Appendix. These cycles
311 are not identical to those of the RMSE, as the approach is different. However, they confirm that using
312 altimetry data and MIOST provides access to the monthly variability of the internal tide. In the next section,
313 we will test the effectiveness of monthly atlases in removing the internal tides from altimetry observations.

314 **4- Impact of internal tide correction in altimetric data: comparison between monthly and annual**
315 **atlases.**
316

317 The variance reduction is a way of measuring how much an internal tide atlas removes or corrects the
318 internal tides in the altimetric SLA. In equation 6, the variance reduction is defined as the difference between
319 the variance of the SLA corrected with the M2 internal tide prediction and the variance of the uncorrected
320 SLA. In this way, a negative value of the variance reduction means that the internal tide atlas has helped to
321 reduce the variance of the SLA. On the other hand, a positive value of the variance reduction means that the
322 internal tide atlas had the opposite effect to what was expected and increased the variance of the SLA.

323 $$variance\ reduction = var\ (SLA - M2\ prediction\ ) - var\ (SLA), (6)$$

324 The annual M2 HRET, MIOST22a, MIOST24a and the monthly M2 MIOST24m atlases are each used in turn
325 as the M2 correction in equation 6, and the monthly variance reductions are calculated in pixels of 0.5° x
326 0.5°. As the main objective is to test the robustness of the monthly atlases, the variance reductions are
327 estimated each month on monthly subsets (see section 1.2) of the altimetry data from period 1 (1993-2017)
328 and period 2 (2018-2023). Examples of variance reduction maps are shown for September only. The atlases
329 are then classified according to the annual cycles of the spatial mean of the monthly variance reduction.

330
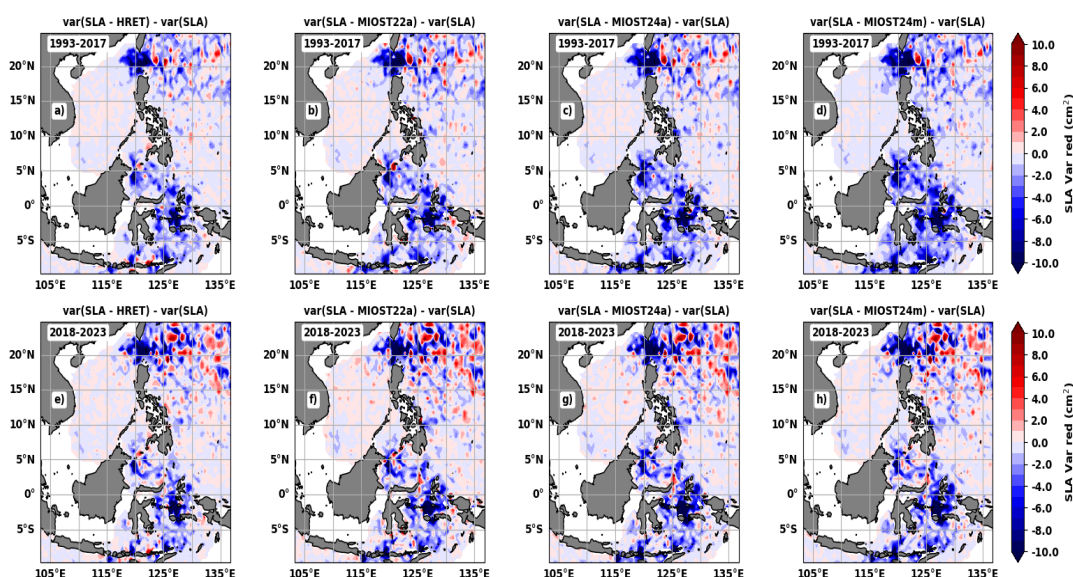
331

332 **Figure 9:** SLA variance reduction (in cm2) in the Indo-Philippine archipelago during September for period 1
333 (a-d, 1993-2017) and period 2 (e-h, 2018-2023).
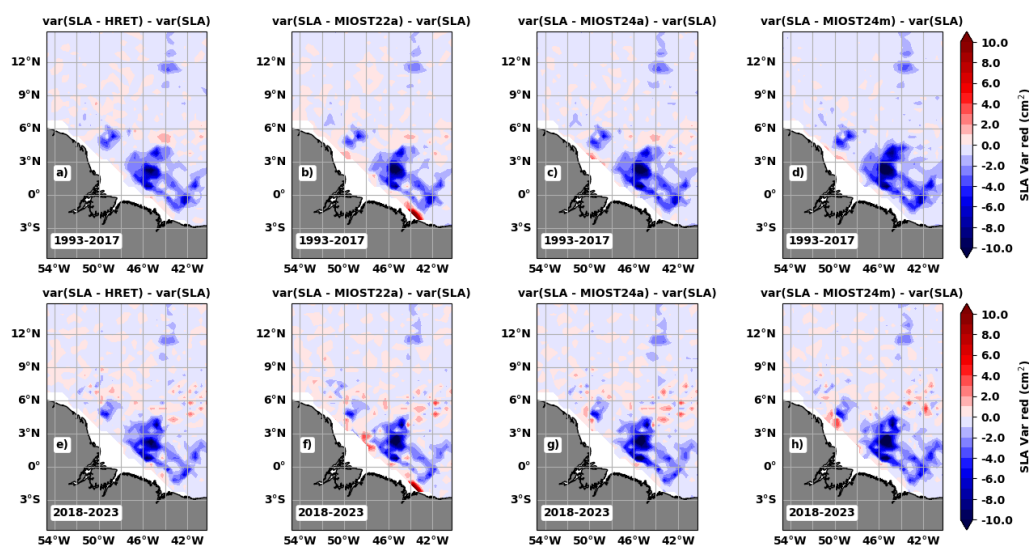
Figure 10: As Figure 9 for the region off the Amazon shelf.

In September (Figure 9), as in other months of the year (not shown), the four atlases performed particularly well around the internal tide generation zones in the Indo-Philippine archipelago, including the Luzon Strait and the entire area south of 10°N (Figure 6).In the Amazon region (Figure 10), the beneficial effects of the atlases in reducing the SLA variance are noticeable in the areas and beams of maximum amplitude of the internal tides previously shown in Figure 7. Some areas, such as the Philippine Sea (Figure 9) and the Amazon shelf-break (Figure 10 b and f), present a local increase in variance due to the internal tides atlases. Compared to period 1 (Figure 9 a-d and Figure 10 a-d), this negative effect of the atlases is more pronounced in period 2 (Figure 9 e-h and Figure 10 e-h). However, in period 2 the atlases still perform well at the locations where the internal tides are generated and along their main trajectories. This indicates that in period 2 the atlases have more difficulty in correcting the incoherent internal tide.

In both regions, the MIOST24m atlas has the best internal tide correction in period 1 (Figure 11 a-b), followed by the MIOST24a atlas. The atlases that eliminate the least variance in period 1 are HRET for the Indo-Philippine archipelago (Figure 11a) and MIOST22a (Figure 11b) for the region off the Amazon shelf. The positions of MIOST24a and MIOST24m are reversed in period 2 in the Indo-Philippine archipelago (Figure 11c), with MIOST24a being slightly better for most months. In the Amazon region (Figure 11d), the MIOST24m atlas outperforms the other atlases between March and June and again between August and November. The positions of MIOST22a and HRET in period 1 are unchanged in period 2.

It is not surprising that the MIOST24 atlases performed better than HRET and MIOST22a in period 1, the variance reductions are indeed calculated on the same dataset used to obtain the MIOST24 atlases. However, the fact that the two MIOST24 atlases perform better on independent period 2 data shows that the wavelengths' change from MIOST22 to MIOST24 has a positive impact on the internal tide correction in the altimetry data. Regarding the use of monthly atlases to correct internal tides in altimetric SLA, our results show that they are appropriate and indicated when applied to the data used to construct them. On an independent dataset, the monthly atlas remains effective at the generation site and on the main trajectories of the internal tide, but it may struggle to correct the internal tides on the secondary trajectories associated with the incoherence of the internal tide. Finally, MIOST22a is the least efficient atlas in the Amazon region because it increases the variance of the SLA along the coast, and in the open ocean it is better than HRET but not than the MIOST24 atlases.
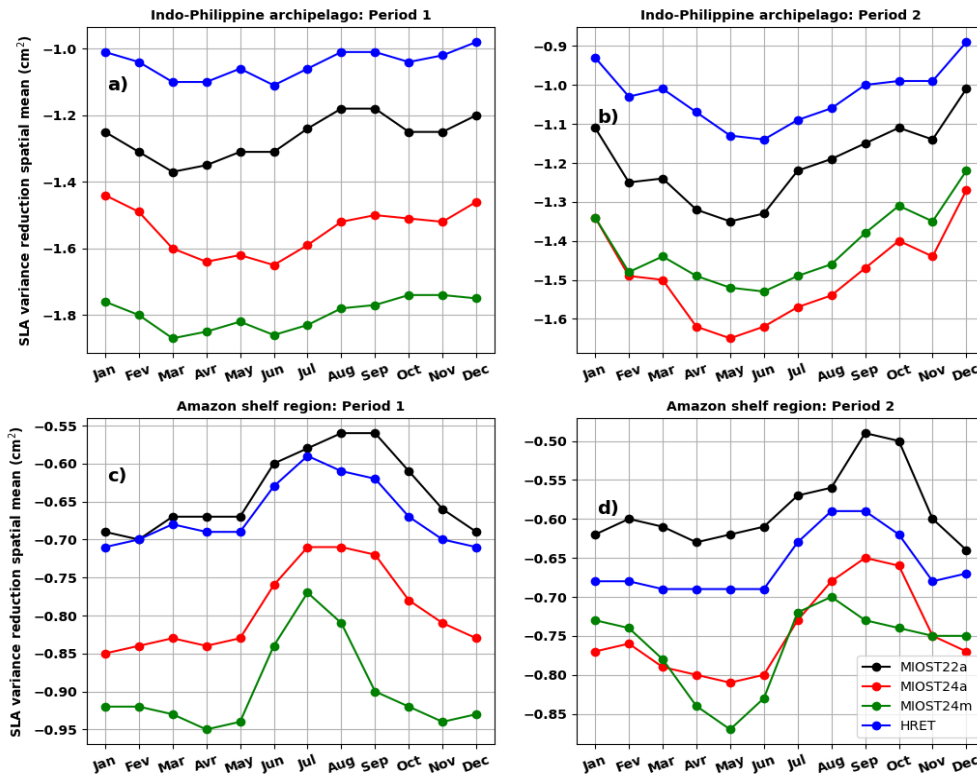
Figure 11: Spatial mean of monthly variance reduction (in cm²) in (left) the Indo-Philippine Archipelago and (right) the region off the Amazon shelf in (top) period 1 (1993-2017) and (bottom) period 2 (2018-2023). The variance reduction was calculated according to equation 6, using either M2 prediction from the MIOST22a (black), HRET (blue), MIOST22a (red) and MIOST24m (green) atlases.

5- Conclusion.

This study presents the M2 MIOST24 (MIOST 2024) internal tide atlas for modes 1 and 2 in the Indo-Philippine archipelago and the region off the Amazon shelf, derived from 25 years (1993-2017) of altimetric SLA and compared with the existing atlases MIOST22 (version 2022, Ubelmann et al., 2022) and HRET (Zaron, 2019). The latest is currently used as the reference atlas for correcting internal tides in altimetry data. The improvement of M2 wavelengths is the distinguishing feature between MIOST24 and MIOST22. MIOST24 uses the M2 wavelengths of modes 1 and 2 obtained after solving the vertical mode equations constrained by the stratification of the 1993-2020 monthly climatologies from the GLORYS12v1 reanalyzes, whereas MIOST22 used the first Rossby deformation radius climatology of Chelton et al. (1998) as an approximation of the mode 1 wavelength, then divided the mode 1 wavelength by 2 to obtain the mode 2 wavelengths. The MIOST24a annual atlas is produced by averaging the GLORYS12v1 monthly reanalyzes and using the altimetry data as a set. In contrast, the MIOST24m monthly atlases are derived from GLORYS12v1 monthly reanalyszes and subsets of altimetry data, defined with a 15-day overlap in each of the months adjacent (see section 1.3) to the month of interest. The differences between MIOST24, MIOST22 and HRET, the monthly variability of the internal tide and the relevance of using a monthly atlas to correct for the internal tide in altimetry data are discussed.

387   The RMSE calculated between M2 atlases of MIOST24a and MIOST22a and between MIOST24a and HRET
388   reaches 3 cm at certain locations in the Indo-Philippine archipelago and the Amazon region, highlighting
389   internal tide estimates that were certainly biased in previous atlases. The spatial mean of the rate of
390   contributions to the RMSE (Rc), defined as the ratio between the contribution of phase differences to the
391   RMSE and the contribution of amplitude differences to the RMSE, shows that the differences between
392   MIOST24a and MIOST22a are mostly explained in the two regions of interest by the phase differences
393   between the two atlases. This means that the differences between the internal tide patterns of MIOST24a
394   and MIOST22a are greater than the differences between the amplitudes of these atlases. This is not surprising
395   as the M2 internal tide structures are better represented in MIOST24a thanks to the improved wavelengths
396   of modes 1 and 2 in MIOST24. The differences between HRET and MIOST24a are related to both amplitude
397   and phase differences. This is because the internal tide amplitudes are larger in MIOST24a and HRET is a
398   smoothed atlas.

399   The amplitude maps of the MIOST24m atlas and the monthly RMSE calculated between MIOST24a and
400   MIOST24m confirm that the M2 internal tides vary over the year. In the Indo-Philippine archipelago, mode
401   1 internal tides generated in the Luzon strait propagate strongly towards the Philippine Sea in the early
402   months of the year (such as April) and in December. In other months, such as June and September, the
403   internal tide structure deforms rapidly. In the South China Sea and the rest of the archipelago, the amplitude
404   and trajectories of the internal tides show significant monthly variability. The total (including modes 1 and 2)
405   internal tide atlases for January and August are the least close to the annual atlas, whereas May is the closest.
406   Mode 2 atlases are distinguished by their amplitude, being furthest from the annual atlas in February and
407   September and closest in July . Overall, for this region, the variability of the monthly atlases has yet to be
408   linked to changes in stratification, seasonal cycles of currents (Sprintall et al., 2019) and seasonal cycles of
409   cyclonic and anticyclonic eddies (Hao et al., 2021), this is beyond the scope of this study and needs special
410   future dedicated study to be revealed.

411   In the Amazon region, our results on the monthly variability of M2 internal tides are in good agreement with
412   those of Tchilibou et al. (2022): from March to June the internal tides propagate far offshore, whereas from
413   August to December the propagation seems to stop at about 5°N. Tchilibou et al (2022) have shown that this
414   is the result of the interaction between internal tides and the mesoscale, which is stronger in the fall season.
415   The RMSE between MIOST24a and MIOST24m allows us to find the bimodal variation MAMJJ (March to July)
416   and ASOND (August to December) of Tchilibou et al. (2022) for mode 1 and the total internal tide, and to
417   show that mode 2 remains relatively stable until April before following the bimodal cycle of mode 1.

418   The annual cycle of the spatial mean of Rc suggests that, in the Indo-Philippine archipelago and the region
419   off the Amazon shelf, for mode 1, the main differences between the annual and monthly atlases result from
420   changes in the phase (*e.i.* the spatial distribution of the M2 internal tides). For mode 2, the annual and
421   monthly atlases are characterized by differences in the internal tide amplitude. The results from these two
422   regions illustrate that altimetry can be used, to some extent at least, to study the monthly variability of the
423   internal tides. In a few years, the monthly atlases could be re-evaluated with longer data series and limiting
424   the overlap of the data from the surrounding months, which may improve furthermore the present results.

425   The last part of the study is devoted to the quantification of the new internal tide correction in the altimetry
426   data : to date, annual atlases (HRET, MIOST22a or MIOST24a) are used instead of monthly atlases
427   (MIOST24m), which are more accurate in terms of the internal tide variability. Variance reductions were
428   calculated for the period (1993-2017, period 1) used to derive the MIOST24 atlases and for an independent
429   period (2018-2023, period 2). For both regions, MIOST24m is the atlas that best corrects the internal tide
430   signal in period 1 altimetry data. In period 2, MIOST24a is better in the Indo-Philippine archipelago, while
431   MIOST24m is better in the region off the Amazon shelf depending on the season. As MIOST24m is not always
432   the best atlas for period 2 in both regions, it is more judicious to choose between annual and monthly atlases
433   depending on the objectives. Monthly atlases are recommended if they are to be applied to the same

434   database from which they were derived as they reflect a specific seasonal variability which can have strong
435   annual variations. On independent data, monthly atlases should work well around the internal tides
436   generation sites and along their main trajectories. Beyond these locations, the performance of the monthly
437   atlases is conditioned by changes in the secondary trajectories reflecting the incoherence of the internal tide.
438   The annual atlas, on the other hand, may underestimate the correction around the generation sites, but
439   make a less degraded correction along the secondary trajectories of the internal tide.

440   In general, the new MIOST24 M2 atlases extract internal tides from altimetric data better than MIOST22
441   and HRET for the Indo-Philippine and Amazon regions. The results of MIOST24 are encouraging and justify
442   the development of a global version of the annual MIOST24 atlas for the M2 wave as well as for the N2, S2,
443   K1 and O1 waves. The new MIOST24 atlas could incorporate satellite data beyond 2017. Initially, the new
444   global atlas will only include the classic nadir missions described in this article. In a second phase, tests could
445   be carried out to incorporate 2D observations from the new SWOT (Surface Water and Ocean Topography)
446   KaRIn mission to improve the spatial resolution of the atlases and its impact on the mode 2 descriptions.

447

448   **Appendix:**

449   **A.1- Example of an annual cycle of mode 1 and 2 M2 wavelengths**

450   The curves of the spatial averages of the monthly M2 wavelengths of mode 1 (in black) and mode 2 (in
451   green) are shown in Figure A1. The spatial means are calculated in the Luzon Strait (Figure A1a), Sulu Island
452   Chain (Figure A1b) and Seram Sea (Figure A1c) boxes as shown in Figure 1. The Amazon region is treated as
453   a box because internal tides generation occurs over almost the entire shelf break, although it is dominant in
454   the six locations shown in Figure 1. The annual cycles of mode 1 and 2 M2 wavelengths are in phase in the
455   Luzon Strait (Figure A1a). Mode 1 increases by an average of 7 km between February (when it is lowest) and
456   September (when it is highest). For mode 2, the variation is about 5 km. In the Sulu Island chain (Figure A1b)
457   and for mode 1, a first peak is observed in June and a second peak in October. Although the cycle of mode 2
458   is close to that of mode 1, the monthly variations remain small (less than 1 km, Figure A1b green curve) and
459   agree with Figure 2f.
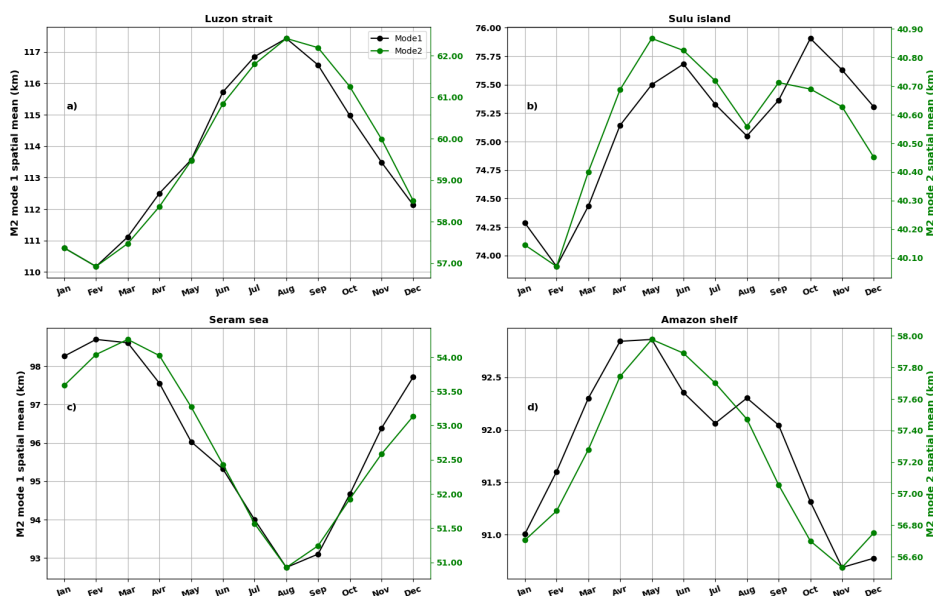
460

461 **Figure A1:** Annual cycle of mode 1 (black) and mode 2 (green) M2 internal tide wavelengths in the Luzon
462 Strait (a), the Sulu Island chain (b), the Serem Sea (c) and the Amazon region (d). The right vertical axis (green)
463 corresponds to mode 2.

464   The annual cycle of M2 wavelengths in the Seram Sea (Figure A1c) is opposite to that observed in the Luzon
465 Strait. The longest wavelengths are observed in March and the shortest in August, representing a variation
466 of more than 4 km for mode 1 and about 3 km for mode 2 (Figure A1c). In the Amazon region (Figure A1d),
467 there are variations of about 2 km for mode 1 and 2 wavelengths, which are the longest between April and
468 May and the shortest in November. However, the spatial mean is certainly influenced by variations in the
469 eastern part of the basin and reduced by small variations in the western part of the basin (Figures 3e and 3f).

470 **A.2- Annual cycle of M2 internal tide amplitude**

471   The annual cycles of the internal tide amplitude M2 are obtained by averaging, as above, the amplitudes
472 of the monthly MIOST24m atlases in the Luzon Strait, the Sulu Island Chain and the Serem Sea for the Indo-
473 Philippine archipelago, and the entire Amazon region. The annual cycles of M2 internal tide amplitudes are
474 represented by black, dashed black and green curves for total tide (mode 1 and 2), mode 1 and 2, respectively.

475   In the Luzon Strait (Fig. A.2a), the amplitude of the internal tides reaches its maximum in October. This
476 maximum of about 4 cm follows a relative maximum of 3.6 cm that occurs in spring (April-May), giving the
477 annual cycle a bimodal appearance. The amplitude of mode 2 is maximum in August and minimum in
478 February. The apparent bimodality of mode 1 could be related to the combination in our Luzon Box of the
479 annual antiphase cycles of the M2 internal tides propagating eastward in the Pacific (Philippine Sea) and
480 westward in the South China Sea, as described in Zhao and Qui (2023). The intense eastward flow in winter
481 and spring is expected to contribute to the relative maximum, while the intense westward flow in summer
482 and autumn helps to increase the mean amplitude to the absolute maximum.

483
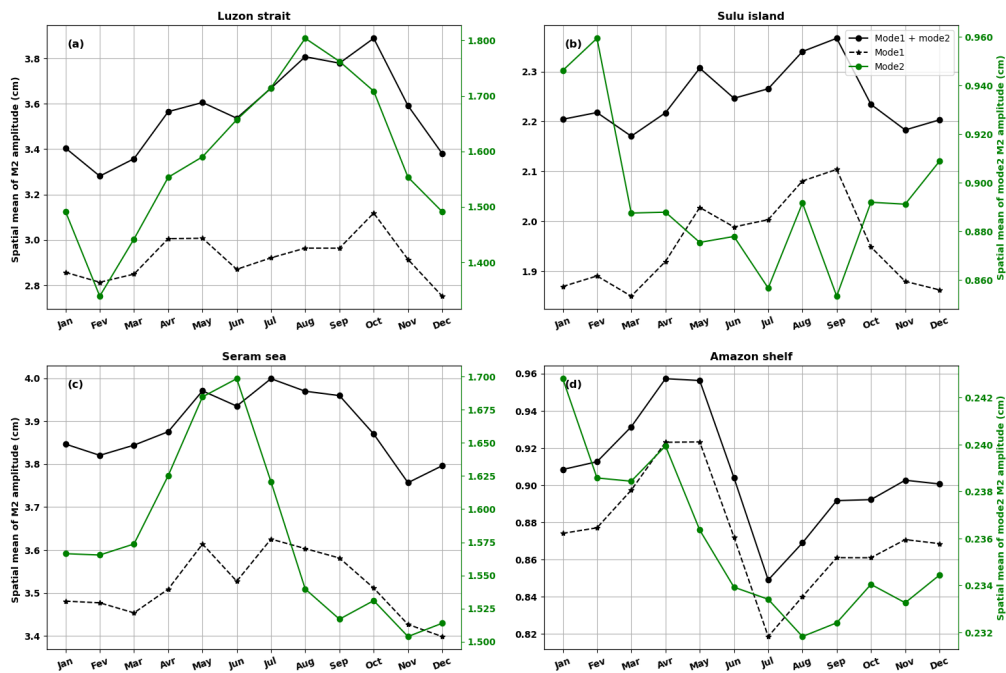
Figure A2: Annual cycle of M2 internal tidal amplitudes in the Luzon Strait (a), the Sulu Island Chain (b), the Serem Sea (c) and the Amazon region (d). In black is the total amplitude including modes 1 and 2, dashed black is mode 1, green is mode 2 and the vertical axis on the right (green) corresponds to mode 2.

In the Sulu Island chain, the annual cycle is bimodal for the total internal tides and mode 1 (Figure A2b). The peaks occur in May and September and are at almost identical levels. The amplitude of mode 2 remains relatively constant, as do the wavelengths of this mode. It cannot be excluded that the shape of the annual cycle of mode 1 in this part of the ocean is related to seasonal divergences in the propagation of internal tides towards the Sulu and Celebes Seas, as observed in Figure 6. In the Seram Sea, the amplitudes of the total and mode 1 internal tide reach their maximum in July, one month later than the mode 2 maximum (Figure A2c). In the second half of the year, the amplitude of the internal tides decreases. The annual cycle is closer to monomodal, although the first maximum for mode 1 occurs in May.

In the Amazon region (Fig. A2d), the internal tides (total and mode 1) are highest between April and May and lowest in July. The distribution of the monthly RMSE in Figure 8b and Tchilibou et al. (2022) is somewhat recovered. The M2 amplitudes are very strong between March and June when the internal tides propagate freely. The weak amplitudes between August and December form a second block of variation. The spatial averages of the mode 2 M2 internal tide amplitude vary between 0.235 and 0.245 cm in the Amazon region. This variation is quite negligible and could be explained by possible compensation for what happens in the different internal tide generation sites. For example, in Figure 7, the transition from April to September is characterized by a decrease in mode 2 amplitude around site B and an increase in amplitude around sites A and E.

All the annual cycles presented confirm that MIOST and altimetry provide some access to the annual variability of the internal tide. However, the cycles presented are sensitive to the area in which the spatial averaging was carried out. They cannot be considered strictly as the annual cycle of the internal tides in these regions. This is one of the reasons why we have not discussed these cycles in the main part of the paper and have not attempted to establish the links between these cycles and variations in ocean stratification and circulation. The main objective of our study remains the production of annual and monthly atlases of internal tides. To gain a better understanding of the annual internal tidal cycles, further studies should be carried out, for example using a high-resolution model that would allow a focus on the locations where internal tides are generated.

References:

Ablain, M., Cazenave, A., Larnicol, G., Balmaseda, M., Cipollini, P., Faugère, Y., Fernandes, M. J., Henry, O., Johannessen, J. A., Knudsen, P., Andersen, O., Legeais, J., Meyssignac, B., Picot, N., Roca, M., Rudenko, S., Scharffenberg, M. G., Stammer, D., Timms, G., and Benveniste, J.: Improved sea level record over the satellite altimetry era (1993–2010) from the Climate Change Initiative project, Ocean Science, 11, 67–82, https://doi.org/10.5194/os-11-67-2015, 2015.

527   Arbic, B., Richman, J., Shriver, J., Timko, P., Metzger, J., and Wallcraft, A.: Global Modeling of Internal Tides
528   Within an Eddying Ocean General Circulation Model, oceanog, 25, 20–29,
529   https://doi.org/10.5670/oceanog.2012.38, 2012.

530   Assene, F., Koch-Larrouy, A., Dadou, I., Tchilibou, M., Morvan, G., Chanut, J., Costa Da Silva, A., Vantrepotte,
531   V., Allain, D., and Tran, T.-K.: Internal tides off the Amazon shelf – Part 1: The importance of the structuring
532   of ocean temperature during two contrasted seasons, Ocean Sci., 20, 43–67,https://doi.org/10.5194/os-20-
533   43-2024, 2024.

534   Barbot, S., Lyard, F., Tchilibou, M., and Carrere, L.: Background stratification impacts on internal tide
535   generation and abyssal propagation in the western equatorial Atlantic and the Bay of Biscay, Ocean Sci.,17,
536   1563–1583, https://doi.org/10.5194/os-17-1563-2021, 2021.

537   Carrere, L., Arbic, B. K., Dushaw, B., Egbert, G., Erofeeva, S., Lyard, F., Ray, R. D., Ubelmann, C.,Zaron, E., Zhao,
538   Z., Shriver, J. F., Buijsman, M. C., and Picot, N.: Accuracy assessment of global internal tide models using
539   satellite altimetry, Ocean Sci., 17, 147–180, https://doi.org/10.5194/os-17-147-2021, 2021.

540   Chelton, D. B., deSzoeke, R. A., Schlax, M. G., El Naggar, K., and Siwertz, N.: Geographical Variability of the
541   First Baroclinic Rossby Radius of Deformation, J. Phys. Oceanogr., 28, 433–460,
542   https://doi.org/10.1175/1520-0485(1998)028<0433:GVOTFB>2.0.CO;2, 1998.

543   Desai, S. D. and Ray, R. D.: Consideration of tidal variations in the geocenter on satellite altimeter
544   observations of ocean tides, Geophysical Research Letters, 41, 2454–2459,
545   https://doi.org/10.1002/2014GL059614, 2014.

546   Dibarboure, G., Pujol, M.-I., Briol, F., Traon, P. Y. L., Larnicol, G., Picot, N., Mertz, F., and Ablain, M.: Jason-2
547   in DUACS: Updated System Description, First Tandem Results and Impact on Processing and Products, Marine
548   Geodesy, 34, 214–241, https://doi.org/10.1080/01490419.2011.584826, 2011.

549   Duda, T. F., Lin, Y.-T., Buijsman, M., and Newhall, A. E.: Internal Tidal Modal Ray Refraction and Energy Ducting
550   in Baroclinic Gulf Stream Currents, J. Phys. Oceanogr., 48, 1969–1993, https://doi.org/10.1175/JPO-D-18-
551   0031.1, 2018.

552   Dunphy, M. and Lamb, K. G.: Focusing and vertical mode scattering of the first mode internal tide by
553   mesoscale eddy interaction: mode one focusing and scattering, J. Geophys. Res.-Oceans, 119, 523–536,
554   https://doi.org/10.1002/2013JC009293, 2014.

555   Dushaw, B. D.: An Empirical Model for Mode-1 Internal Tides, Applied Physics Laboratory University of
556   Washington, 2015.

557   Dushaw, B. D., Worcester, P. F., and Dzieciuch, M. A.: On the predictability of mode-1 internal tides, Deep
558   Sea Research Part I: Oceanographic Research Papers, 58, 677–698,
559   https://doi.org/10.1016/j.dsr.2011.04.002, 2011.

560   Egbert, G. D. and Erofeeva, S. Y.: Efficient inverse modeling of barotropic ocean tides, J. Atmos. Oceanic
561   Technol., 19, 183–204,2002.

562   Escudier, P., Couhert, A., Mercier, F., Mallet, A., Thibaut, P., Tran, N., Amarouche, L., Picard, B., Carrere, L.,
563   and Dibarboure, G.: Satellite Radar Altimetry: Principle, Accuracy, and Precision, in: Satellite Altimetry Over
564   Oceans and Land Surfaces, CRC Press, 2017.

565   Faugère, Y., Taburet, G., Ballarotta, M., Pujol, I., Legeais, J. F., Maillard, G., Durand, C., Dagneau, Q.,Lievin,
566   M., Roman, A. S., and Dibarboure, G.: DUACS DT2021: 28 years of reprocessed sea level altimetry products,
567   Copernicus Meetings, https://doi.org/10.5194/egusphere-egu22-7479, 2022.

568 Gerkema, T., Lam, F. A., and Maas, L. R. M.: Internal tides in the Bay of Biscay: conversion rates and seasonal
569 effects, Deep Sea Research Part II: Topical Studies in Oceanography, 51, 2995–
570 3008,https://doi.org/10.1016/j.dsr2.2004.09.012, 2004.

571 Gill, A.: Atmosphere-Ocean Dynamics, 1st edition., Academic Press, New York, 680 pp., 1982.

572 Hao, Z., Xu, Z., Feng, M., Li, Q., and Yin, B.: Spatiotemporal Variability of Mesoscale Eddies in the Indonesian
573 Seas, Remote Sensing, 13, 1017, https://doi.org/10.3390/rs13051017, 2021.

574 Hurlburt, H., Metzger, J., Sprintall, J., Riedlinger, S., Arnone, R., Shinoda, T., and Xu, X.: Circulation in the
575 Philippine Archipelago Simulated by 1/12° and 1/25° Global HYCOM and EAS NCOM, Oceanog, 24, 28–47,
576 https://doi.org/10.5670/oceanog.2011.02, 2011.

577 Jan, S., Lien, R.-C., and Ting, C.-H.: Numerical study of baroclinic tides in Luzon Strait, J Oceanogr, 64, 789–
578 802, https://doi.org/10.1007/s10872-008-0066-5, 2008.

579 Koch-Larrouy, A., Lengaigne, M., Terray, P., Madec, G., and Masson, S.: Tidal mixing in the Indonesian Seas
580 and its effect on the tropical climate system, Clim Dyn, 34, 891–904, https://doi.org/10.1007/s00382-009-
581 0642-4, 2010.

582 Kocha. C. , Y. Pageot, C. Rubin , M . Lievin , M-I. Pujol , S. Philipps, P. Prandi , S. Labroue, I. Denis , G.
583 Dibarboure , C. Nogueira Loddo.: 30 years of sea level anomaly reprocessed to improve climate and
584 mesoscale satellite data record. Presented at the 2023 Ocean Surface Topography Science Team meeting:
585 https://doi.org/10.24400/527896/a03-2023.3805, 2023

586 Lyard, F. H., Allain, D. J., Cancet, M., Carrère, L., and Picot, N.: FES2014 global ocean tide atlas: design and
587 performance, Ocean Science, 17, 615–649, https://doi.org/10.5194/os-17-615-2021, 2021.

588 Niwa, Y. and Hibiya, T.: Numerical study of the spatial distribution of the M2 internal tide in the Pacific Ocean,
589 J. Geophys. Res., 106, 22441–22449, https://doi.org/10.1029/2000JC000770, 2001.

590 Niwa, Y. and Hibiya, T.: Three-dimensional numerical simulation of M2 internal tides in the East China Sea, J.
591 Geophys. Res., 109, 2003JC001923, https://doi.org/10.1029/2003JC001923, 2004.

592 Niwa, Y. and Hibiya, T.: Generation of baroclinic tide energy in a global three-dimensional numerical model
593 with different spatial grid resolutions, Ocean Modelling, 80, 59–73,
594 https://doi.org/10.1016/j.ocemod.2014.05.003, 2014.

595 Nugroho, D.: La marée dans un modèle de circulation générale dans les mers indonésiennes, These de
596 doctorat, Toulouse 3, 2017.

597 Nugroho, D., Koch-Larrouy, A., Gaspar, P., Lyard, F., Reffray, G., and Tranchant, B.: Modelling explicit tides in
598 the Indonesian seas: An important process for surface sea water properties, Marine Pollution Bulletin, 131,
599 7–18, https://doi.org/10.1016/j.marpolbul.2017.06.033, 2018.

600 Pickering, A., Alford, M., Nash, J., Rainville, L., Buijsman, M., Ko, D. S., and Lim, B.: Structure and Variability of
601 Internal Tides in Luzon Strait, Journal of Physical Oceanography, 45, 1574–1594,
602 https://doi.org/10.1175/JPO-D-14-0250.1, 2015.

603 Pujol, M.-I., Faugère, Y., Taburet, G., Dupuy, S., Pelloquin, C., Ablain, M., and Picot, N.: DUACS DT2014: the
604 new multi-mission altimeter data set reprocessed over 20years, Ocean Sci., 12, 1067–
605 1090,https://doi.org/10.5194/os-12-1067-2016, 2016.

606 Pujol, M.-I., Dupuy, S., Vergara, O., Sánchez Román, A., Faugère, Y., Prandi, P., Dabat, M.-L., Dagneaux, Q.,
607 Lievin, M., Cadier, E., Dibarboure, G., and Picot, N.: Refining the Resolution of DUACS Along-Track Level-3 Sea
608 Level Altimetry Products, Remote Sensing, 15, 793, https://doi.org/10.3390/rs15030793, 2023.

609 Rainville, L. and Pinkel, R.: Propagation of Low-Mode Internal Waves through the Ocean, Journal of Physical
610 Oceanography, 36, 1220–1236, https://doi.org/10.1175/JPO2889.1, 2006.

611 Rainville, L., Lee, C. M., Rudnick, D. L., and Yang, K.: Propagation of internal tides generated near Luzon Strait:
612 Observations from autonomous gliders, JGR Oceans, 118, 4125–4138, https://doi.org/10.1002/jgrc.20293,
613 2013.

614 Ray, R. D. and Zaron, E. D.: Non-stationary internal tides observed with satellite altimetry:
615 NONSTATIONARYINTERNAL TIDES, Geophys. Res. Lett., 38, n/a-n/a, https://doi.org/10.1029/2011GL048617,
616 2011.

617 Ray, R. D. and Zaron, E. D.: M2 Internal Tides and Their Observed Wavenumber Spectra from Satellite
618 Altimetry, Journal of Physical Oceanography, 46, 3–22, https://doi.org/10.1175/JPO-D-15-0065.1, 2016.

619 Sánchez-Román, A., Pujol, M. I., Faugère, Y., and Pascual, A.: DUACS DT2021 reprocessed altimetry improves
620 sea level retrieval in the coastal band of the European seas, Ocean Sci., 19, 793–809,
621 https://doi.org/10.5194/os-19-793-2023, 2023.

622 Sprintall, J., Gordon, A. L., Koch-Larrouy, A., Lee, T., Potemra, J. T., Pujiana, K., and Wijffels, S. E.: The
623 Indonesian seas and their role in the coupled ocean–climate system, Nature Geosci, 7, 487–
624 492,https://doi.org/10.1038/ngeo2188, 2014.

625 Sprintall, J., Gordon, A. L., Wijffels, S. E., Feng, M., Hu, S., Koch-Larrouy, A., Phillips, H., Nugroho, D., Napitu,
626 A., Pujiana, K., Susanto, R. D., Sloyan, B., Peña-Molino, B., Yuan, D., Riama, N. F., Siswanto, S., Kuswardani,
627 A., Arifin, Z., Wahyudi, A. J., Zhou, H., Nagai, T., Ansong, J. K., Bourdalle-Badié, R., Chanut, J., Lyard, F., Arbic,
628 B. K., Ramdhani, A., and Setiawan, A.: Detecting Change in the Indonesian Seas, Front. Mar. Sci., 6, 257,
629 https://doi.org/10.3389/fmars.2019.00257, 2019.

630 Stammer, D., Ray, R. D., Andersen, O. B., Arbic, B. K., Bosch, W., Carrère, L., Cheng, Y., Chinn, D. S., Dushaw,
631 B. D., Egbert, G. D., Erofeeva, S. Y., Fok, H. S., Green, J. a. M., Griffiths, S., King, M. A., Lapin, V., Lemoine, F.
632 G., Luthcke, S. B., Lyard, F., Morison, J., Müller, M., Padman, L., Richman, J. G., Shriver, J. F., Shum, C. K.,
633 Taguchi, E., and Yi, Y.: Accuracy assessment of global barotropic ocean tide models, Reviews of Geophysics,
634 52, 243–282, https://doi.org/10.1002/2014RG000450, 2014.

635 Tchilibou, M., Gourdeau, L., Lyard, F., Morrow, R., Koch Larrouy, A., Allain, D., and Djath, B.: Internal tides in
636 the Solomon Sea in contrasted ENSO conditions, Ocean Sci., 16, 615–635, https://doi.org/10.5194/os-16-
637 615-2020, 2020.

638 Tchilibou, M., Koch-Larrouy, A., Barbot, S., Lyard, F., Morel, Y., Jouanno, J., and Morrow, R.: Internal tides off
639 the Amazon shelf during two contrasted seasons: interactions with background circulation and SSH imprints,
640 Ocean Sci., 18, 1591–1618, https://doi.org/10.5194/os-18-1591-2022, 2022.

641 Ubelmann, C., Dibarboure, G., Gaultier, L., Ponte, A., Ardhuin, F., Ballarotta, M., and Faugère, Y.:
642 Reconstructing Ocean Surface Current Combining Altimetry and Future Spaceborne Doppler Data, JGR
643 Oceans, 126, e2020JC016560, https://doi.org/10.1029/2020JC016560, 2021.

644 Ubelmann, C., Carrere, L., Durand, C., Dibarboure, G., Faugère, Y., Ballarotta, M., Briol, F., and Lyard, F.:
645 Simultaneous estimation of ocean mesoscale and coherent internal tide sea surface height signatures from
646 the global altimetry record, Ocean Sci., 18, 469–481, https://doi.org/10.5194/os-18-469-2022, 2022.

647 Zaron, E. D.: Baroclinic Tidal Sea Level from Exact-Repeat Mission Altimetry, Journal of Physical
648 Oceanography, 49, 193–210, https://doi.org/10.1175/JPO-D-18-0127.1, 2019.

649 Zhao, Z.: The Global Mode-2 M2 Internal Tide, JGR Oceans, 123, 7725–7746,
650 https://doi.org/10.1029/2018JC014475, 2018.

651   Zhao, Z.: Mapping Internal Tides From Satellite Altimetry Without Blind Directions, JGR Oceans, 124, 8605–
652   8625, https://doi.org/10.1029/2019JC015507, 2019.

653   Zhao, Z.: Seasonal mode-1 M2 internal tides from satellite altimetry, Journal of Physical
654   Oceanography,https://doi.org/10.1175/JPO-D-21-0001.1, 2021.

655   Zhao, Z. and Qiu, B.: Seasonal West-East Seesaw of M2 Internal Tides From the Luzon Strait, Journal of
656   Geophysical Research: Oceans, 128, e2022JC019281, https://doi.org/10.1029/2022JC019281, 2023.

657   Zhao, Z., Alford, M., and Girton, J.: Mapping Low-Mode Internal Tides from Multisatellite Altimetry, oceanog,
658   25, 42–51, https://doi.org/10.5670/oceanog.2012.40, 2012.